RESEARCH

Open Access

Spatiotemporal dynamics of early oogenesis in pigs

Wei Ge[1*], Yi-Lin Niu[1], Yu-Kang Li[1], Li Li[1], Han Wang[1], Wen-Wen Li[1], Tian Qiao[1], Yan-Ni Feng[2], Yu-Qing Feng[3], Jing Liu[4], Jun-Jie Wang[1], Xiao-Feng Sun[1], Shun-Feng Cheng[1], Lan Li[1] and Wei Shen[1*]

*Correspondence:
gewei0901@qau.edu.cn;
wshen@qau.edu.cn

[1] College of Life Sciences,
Key Laboratory of Animal
Reproduction and Biotechnology
in Universities of Shandong,
Qingdao Agricultural University,
Qingdao 266109, China
[2] Laboratory of Animal
Reproductive Physiology
and Disease, College
of Veterinary Medicine,
Qingdao Agricultural University,
Qingdao 266109, China
[3] School Hospital, Qingdao
Agricultural University,
Qingdao 266109, China
[4] Central Laboratory of Qingdao
Agricultural University, Qingdao
Agricultural University,
Qingdao 266109, China

Abstract

Background: In humans and other mammals, the process of oogenesis initiates asynchronously in specific ovarian regions, leading to the localization of dormant and growing follicles in the cortex and medulla, respectively; however, the current understanding of this process remains insufficient.

Results: Here, we integrate single-cell RNA sequencing (scRNA-seq) and spatial transcriptomics (ST) to comprehend spatial–temporal gene expression profiles and explore the spatial organization of ovarian microenvironments during early oogenesis in pigs. Projection of the germ cell clusters at different stages of oogenesis into the spatial atlas unveils a "cortical to medullary (C-M)" distribution of germ cells in the developing porcine ovaries. Cross-species analysis between pigs and humans unveils a conserved C-M distribution pattern of germ cells during oogenesis, highlighting the utility of pigs as valuable models for studying human oogenesis in a spatial context. RNA velocity analysis with ST identifies the molecular characteristics and spatial dynamics of granulosa cell lineages originating from the cortical and medullary regions in pig ovaries. Spatial co-occurrence analysis and intercellular communication analysis unveils a distinct cell–cell communication pattern between germ cells and somatic cells in the cortex and medulla regions. Notably, in vitro culture of ovarian tissues verifies that intercellular NOTCH signaling and extracellular matrix (ECM) proteins played crucial roles in initiating meiotic and oogenic programs, highlighting an underappreciated role of ovarian microenvironments in orchestrating germ cell fates.

Conclusions: Overall, our work provides insight into the spatial characteristics of early oogenesis and the regulatory role of ovarian microenvironments in germ cell fate within a spatial context.

Keywords: Spatiotemporal transcriptomics, Early oogenesis, Microenvironments

Background

A key histological feature of the developing mammalian ovary is that dormant follicles are located in the outer region of the ovarian cortex, while the growing follicles are predominantly located in the medulla [1, 2]. Using lineage tracing approaches, it has now

been demonstrated that these distinct locations hold different biological significance for the female: follicles located in the medulla region (alternatively, wave I follicles) are critical for the onset of fertility in females, while follicles in the cortical region (alternatively, wave II follicles) determine the duration of fertility in females [3, 4]. However, our current understanding of the spatial organization of ovarian architecture during embryonic stages remains unclear, primarily due to its occurrence during the embryonic stages and orchestration by multiple heterogeneous cell types.

In mice, after the arrival of primordial germ cells (PGCs) at around E10.5 from the extraembryonic mesoderm into the genital ridges [5, 6], they rapidly populate the developing gonad as they undergo several rounds of cell division. The current consensus suggests that germ cells initiate meiosis asynchronously along the anterior to posterior (AP) axis at E13.5, a process partially explained by meiotic inducer retinoic acid (RA) secreted by the mesonephros [7–9]. Notably, a more recent study has revealed that meiotic programs are initiated in the murine ovary in an anterior-radial manner before the AP meiotic wave [10], a process that cannot be explained by classical RA signaling, but by the formation of intercellular bridges via TEX14. Using a *Tex14* (essential for intercellular bridge formation) [11] deficiency mouse model, the AP wave of meiotic initiation can be observed, but not the radial wave. Together, these findings suggest that microenvironments surrounding germ cells also play a crucial role in determining their developmental fate, and unveiling the machinery underlying the spatial positioning of germ cells in the ovary will broaden our understanding of how ovarian architecture correlates with female fertility.

To date, our knowledge of the developing ovary during critical stages of oogenesis predominantly focused on the gene expression profiles and global location of heterogenous germ cell populations in the ovary. However, our understanding of the finer spatial location of germ cells en route to folliculogenesis and the spatial dynamics of other major somatic cell types in the ovary remains limited. To this end, using the cutting-edge ST and scRNA-seq technologies, we herein report a spatiotemporal transcriptomic atlas for early gonad development in pigs. Through the spatial mapping of germ cells and somatic cell types at different stages of development, we have unveiled a corticomedullary gradient of early oogenesis in pigs and characterized the spatial dynamics of somatic cell lineages in the same period. Applying cross-species analysis utilizing ST data from humans and pigs, we observed conservation in the spatial location of germ cells at different stages of oogenesis within the ovaries. Additionally, combined spatial co-occurrence analysis and cell–cell communication analysis unveiled a distinct intracellular communication pattern between germ cells and somatic cells in the cortex and medulla, highlighting the crucial role of ovarian microenvironments on germ cell fate determination.

Results

Construction of a single-cell atlas for early oogenesis in pigs

To reveal the spatiotemporal developmental profiles for early oogenesis in porcine ovaries, we combined scRNA-seq with the cutting-edge $10 \times$ Visium ST technology to systematically dissect the spatial attributes of cells in developing porcine ovaries. Four developmental time points (E45, E55, E65, and E75; for scRNA-seq, 2 embryos each; for ST, E45, E55, E65, two embryos, E75, 1 embryo) were included which covered the stages

Ge *et al. Genome Biology*   (2025) 26:2

Page 3 of 27

of early oogenesis (Fig. 1a). To increase the fidelity of the integrated analysis of scRNA-seq and ST data and to eliminate individual differences, for two ovaries from the same embryo, one was used for scRNA-seq, while the other was used for ST. After stringent quality control and the removal of potential doublets (Additional file 1: Fig. S1a–b), a total of 18,956 high-quality cells were retained for downstream analysis (E45, 4397 cells; E55, 4919 cells; E65, 3480 cells; E75, 6160 cells).

Next, to explore cellular heterogeneity within the developing porcine ovaries, we integrated scRNA-seq data from E45-E75 porcine ovaries and performed uniform manifold approximation and projection (UMAP) analysis; a total of 17 clusters were identified. An in-depth analysis of cluster-specific marker expression revealed 9 major cell types in varying proportions (Fig. 1b; Additional file 1: Fig. S1c–d), including germ cells (*DAZL*, *DDX4*) [12], bipotential pregranulosa (BPG) cells (*WNT6*) [4], epithelial pregranulosa
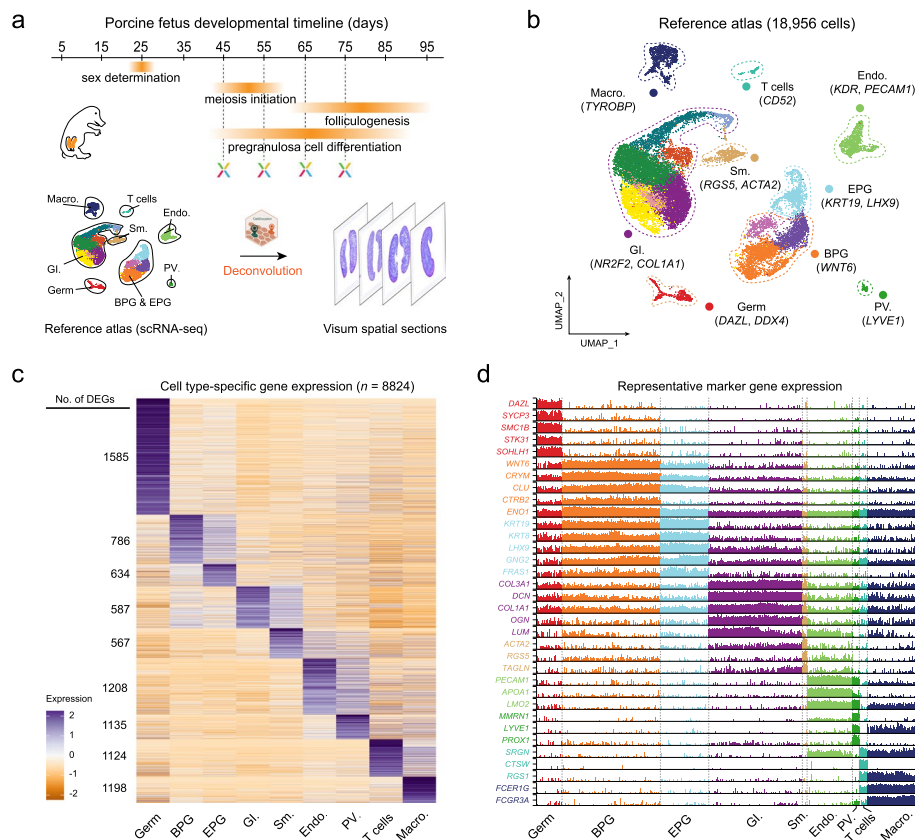

Fig. 1 scRNA-seq of the developing porcine ovary. **a** A brief scheme depicting study design and sampling information. Four developmental time points spanning meiosis prophase I and early folliculogenesis were included. The scRNA-seq libraries from E45 to E75 were constructed using tissues from two independent embryos, and for each embryo, one ovary tissue was used for scRNA-seq, while the other was used for ST to enhance the accuracy of cell type deconvolution. For ST, E45-E65 contains two ovary sections from two independent embryos, and E75 contains one ovarian section due to the chip size. **b** UMAP plot showing different cell clusters annotated by canonical marker gene expression. BPG, biopotential pregranulosa; EPG, epithelial pregranulosa; GI, gonadal interstitial; PV, perivascular; Sm, smooth muscle; Endo, endothelial; Macro, macrophage. **c** Heatmap demonstrating cell-type specific marker gene expression across different cell populations. Numbers on the left indicate the number of identified cell cluster-specific expressed genes. **d** Trackplot demonstrating representative marker gene expression for each cell type

Ge *et al. Genome Biology*   (2025) 26:2

Page 4 of 27

(EPG) cells (*KRT19*, *LHX9*), gonadal interstitial (GI) cells (*NR2F2*, *COL1A1*), smooth muscle (Sm) cells (*RGS5*, *ACTA2*), endothelial (Endo) cells (*KDR*, *PECAM1*), perivascular (PV) cells (*LYVE1*), T cells (*CD52*), and macrophage (Macro) cells (*TYROBP*) [4, 13]. By analyzing the cell-type-specific gene expression profiles, we obtained a total of 8824 characteristic genes for each cell type (Fig. 1c; Additional file 2: Table S1). Additionally, further comparison of their gene expression profiles across all cell types revealed a high degree of cell-type specificity (Fig. 1c–d). Moreover, we performed gene ontology (GO) enrichment analysis for cell type-specific marker genes and the results also showed cell type-specific enrichment of related GO terms. For example, germ cell clusters enriched GO terms of "gamete generation" and "meiotic cell cycle" (Additional file 1: Fig. S1e). Noteworthy, in addition to germ cells, most somatic cells are enriched in GO terms related to "chemotaxis" and "tissue morphogenesis," which to some extent enhances the process of tissue remodeling during pig oogenesis.

Cell-type deconvolution of the spatially resolved porcine ovary transcriptome

scRNA-seq provides unparalleled tools to dissect cellular heterogeneity within complex tissues, while the spatial location of cells is lost during tissue dissociation [14, 15]. To better reveal the spatial scale dynamic changes of different cell types during early ovarian development in pigs, we next utilized Visium ST technology to perform ST sequencing on ovarian tissues at different stages. In total, we obtained 7 ovarian sections using 4 Visium chips spanning 4 developmental time points (Fig. 2a). After sequencing, we first evaluated the quality metrics for each chip and the results showed mean reads of 253,572, 283,276, 163,223, and 258,977 reads per spot and a median of 8730, 9234, 9977, and 12,821 unique molecular identifier (UMI) counts per spot for E45-E75 ovarian samples, respectively (Additional file 1: Fig. S2a–b). Overall, all samples were qualified for downstream analysis.

Currently, the spot size of Visium ST technology is ~ 55 μm, which is larger than the average size of mammalian cells [16]. Therefore, we next used the scRNA-seq data as a reference to perform cell-type deconvolution of the ST data to achieve fine-scale localization analysis using the Cell2location algorithm (Fig. 2a) [17]. Cell-type deconvolution allows the high-resolution location of reference cell types in a spatial context, which gives an unparalleled opportunity to explore gene expression profiles in situ [18]. After cell type deconvolution, we noted that the spatial distribution of cell types was generally "random" at the E45 and E55 (Fig. 2b). Notably, as development progressed to E65, we observed a distinct spatial pattern in the distribution of cell types. Specifically, germ cells at E45-E55 showed a "random" spatial location in the porcine ovary, while for the E65-E75 ovaries, germ cells were predominantly located in the cortex region, with a small proportion located in the medulla region (Fig. 2c, top panel). For pregranulosa cell populations, two types with distinct spatial location patterns were observed (Fig. 2c, middle and bottom panel). BPG cells showed a "random" spatial location before E55 and gradually centralized within the medulla region at E75; meanwhile, EPG cells were located at the ovarian surface across the four stages. Other somatic cells, including GI and Sm, also showed a spatial organization pattern resembling BPG (Additional file 1: Fig. S2c), while the remaining cell types mainly exhibited "random" spatial location pattern.
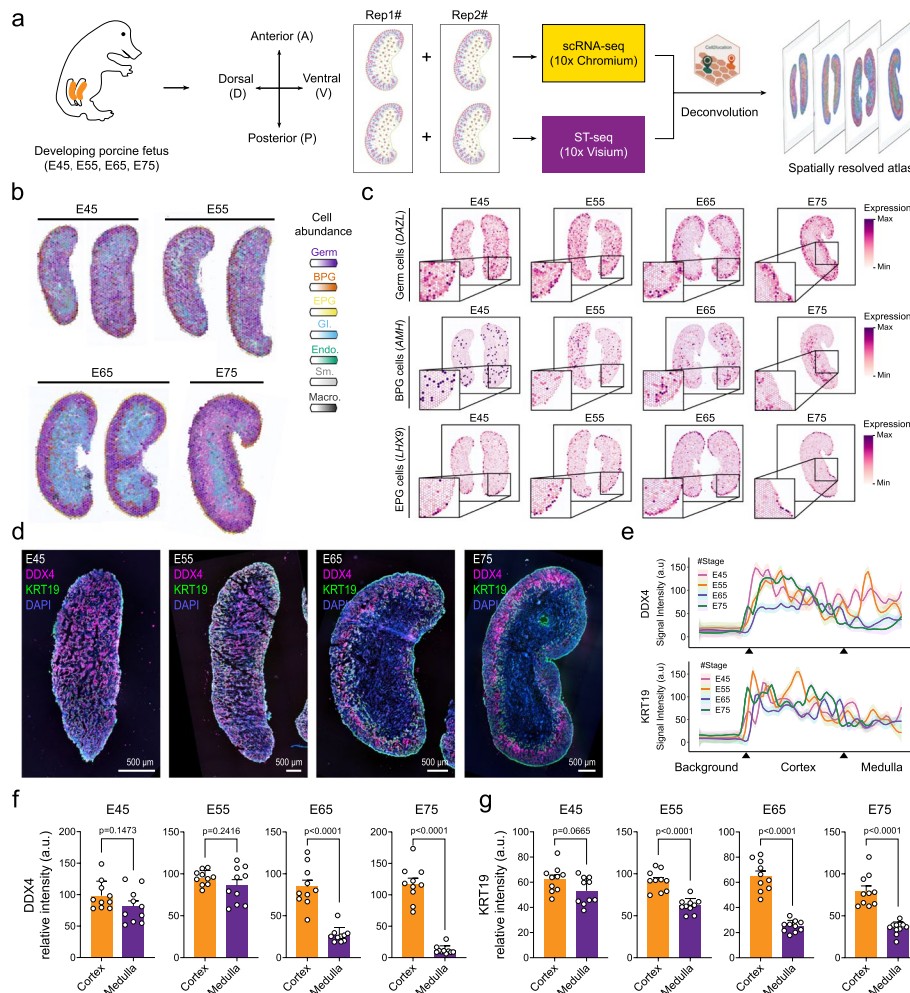
Fig. 2 Deconvolution of ST based on scRNA-seq using Cell2location. **a** A brief scheme illustrating the cell type deconvolution procedure using Cell2location. **b** Estimated cell abundances (revealed by color intensity) of seven major cell types across four developmental time points. **c** Visualization of the spatial gene expression pattern of the canonical marker gene in germ cells, BPG, and EPG across four developmental time points. The intensity of color represents the relative level of gene expression. **d** Whole-mount staining assay of germ cell marker DDX4 (magenta) and EPG marker KRT19 (green) using ovaries from E45-E75 fetal porcine ovaries. DAPI was used to stain nuclei. Scale bars, 500 μm. **e** Comparative analysis of DDX4 (top panel) and KRT19 (bottom panel) fluorescence intensity along the ovarian dorsal–ventral axis. The triangular in the x-axis from left to right represents the position of the ovarian surface and the boundary between the cortex and medulla regions, and the distance was normalized by the ovarian width. For each group, at least five random linear fluorescence intensity profiles were measured and the shaded regions around the curves depict the 95% confidence intervals. **f** The comparative analysis of DDX4 fluorescence staining signal intensity between the cortex and medulla regions was conducted. Ten regions of interest (ROI) were captured for each group using ImageJ. Data are presented as mean ± SEM. **g** The comparative analysis of KRT19 fluorescence staining signal intensity between the cortex and medulla regions was conducted. Ten ROI were captured for each group using ImageJ. Data are presented as mean ± SEM

To further verify our analysis, we performed a whole-mount staining assay of germ cell marker DDX4 and EPG marker KRT19 using fetal ovaries collected from E45 to E75 porcine embryos (Fig. 2d). Consistent with our ST data interpretation, DDX4-positive germ cells were located randomly in the E45 and E55 fetal ovaries, while in the E65 and E75 ovaries, they were predominantly located in the cortex region. For the KRT19-positive

EPG cells, their prominent location on the ovarian surface can be observed, which was also consistent with our ST data analysis. Furthermore, we analyzed the spatial distribution of DDX4 and KRT19-positive cells in transverse sections along the dorsal–ventral axis of E55 and E75 formalin-fixed paraffin-embedded ovaries (Additional file 1: Fig. S2d); the results were consistent with the spatial distribution pattern observed in the sections along the dorsal–ventral axis at the corresponding developmental time points. Next, we evaluated their location pattern by comparing the fluorescence intensity along the dorsal–ventral axis. This analysis further confirmed that DDX4 signals were predominantly higher in the ovarian cortex and decreased in the medulla region at E65 to E75 porcine ovaries (Fig. 2e). For the KRT19 signals, we observed high signal intensity in the ovarian surface and the boundary regions between the ovarian cortex and medulla regions at E65 and E75, which was different from the location pattern of germ cells. Finally, we statistically compared the location pattern of germ cells and EPG in the cortex and medulla regions. Comparing the fluorescence intensity in different regions of interest (ROI, for each group, ten randomly selected ROIs were analyzed) between the ovarian cortex and medulla region (Fig. 2f–g), it was observed that statistically different locations of DDX4 occurred during the E55-E65 stage, while for the EPG cells, the statistically differential location of KRT19 occurred during the E45-E55 stage, preceding the difference observed in germ cells.

Spatially resolved developmental trajectory of fine-scale porcine germ cells

To provide an in-depth understanding of germ cell development in a spatial context, we extracted germ cells and reperformed cell clustering analysis using UMAP (Fig. 3a). Fine-scale analysis of the germ cell populations revealed five clusters corresponding to mitotic fetal germ cells (FGC_mitotic, expressing *TOP2A*, *CCNB1*), pre-meiotic germ cells (Oogonia_STRA8, expressing *MECOM*, *ATM*), meiotic germ cells (Oogonia_meiotic, expressing *SYCP1*, *DMC1*), early oocytes (Pre_oocyte, expressing *FIGLA*, *NANOS1*), and oocytes (Oocyte, expressing *ZP4*, *ZP3*) according to their representative marker expression (Fig. 3b) [19]. By analyzing cluster-specific gene expression profiles, we further identified a series of stage-specific markers during early oogenesis in pigs (Additional file 1: Fig. S3a, Additional file 3: Table S2). Furthermore, GO enrichment analysis using stage-specific markers showed that FGC_mitotic cells enriched in GO terms of "cell division" and "mitotic cell cycle," while Oogonia_STRA8 cells enriched in GO terms of "stem cell differentiation" and "embryonic morphogenesis." Oogonia_meiotic cells enriched in GO terms of "meiotic nuclear division" and "synaptonemal complex organization," and Pre_oocyte enriched in GO terms of "oogenesis" and "female gamete generation." At the Oocyte stage, GO terms of "establishment of spindle localization" and "regulation of reproductive process" were enriched, which also showed consistency with our cell type characterization. Together, these data here provide a valuable resource for unveiling the gene cascades underlying early porcine oogenesis.

To gain further insight into the functional enrichments of module genes across different stages of early porcine oogenesis, we next employed the Hotspot algorithm to identify gene modules of correlated genes using scRNA-seq data of germ cells [20]. In total, Hotspot analysis identified 11 functionally diverse gene modules during early porcine oogenesis (Fig. 3c). Projection of the individual module into the UMAP plot identified
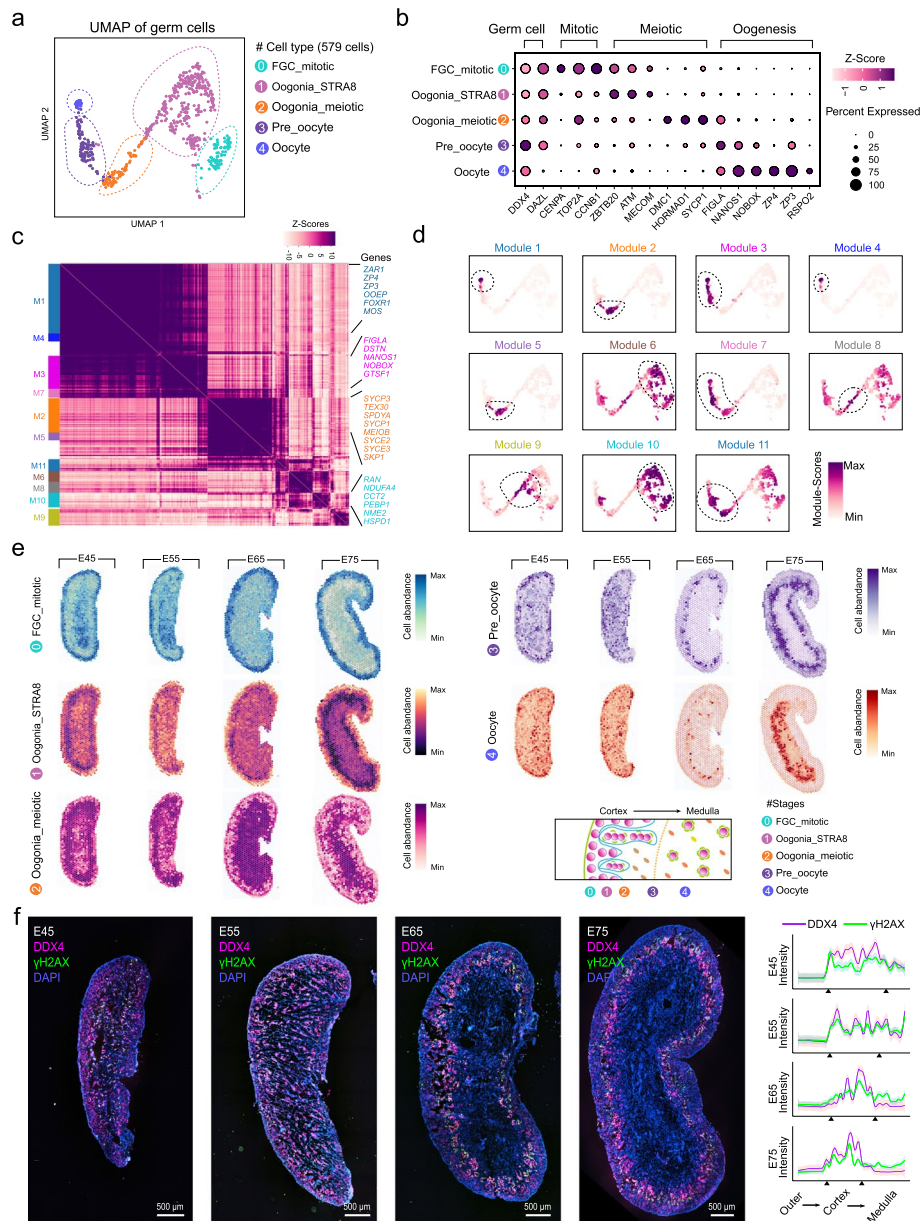
Ge *et al. Genome Biology*   (2025) 26:2

Page 7 of 27

Fig. 3 Characterization of germ cell spatial location pattern using ST. **a** Fine-scale characterization of germ cell subclusters at the early stage of oogenesis in pigs. FGC_mitotic, mitotic germ cells; Oogonia_STRA8, pre-meiotic germ cells; Oogonia_meiotic, meiotic germ cells; Pre_oocyte, early oocytes. **b** Dot plot illustrating stage-specific marker gene expression across germ cell subclusters. **c** Correlation heatmap of functional gene modules identified by Hotspot analysis. Representative module genes were colored-coded in the right panel. **d** Scoring of Hotspot-identified gene modules in the UMAP plot. **e** Estimated abundance (revealed by color intensity) of germ cells at different developmental stages across four developmental time points. The schematic diagram in the bottom right corner illustrates the relative spatial location of germ cell subclusters at different stages in the ovary. **f** Left panel: Characterization of leptotene stage germ cells in situ by whole-mount co-staining of DDX4 (magenta) and γH2AX (green). DAPI was used to stain nuclei. Scale bars, 500 μm. Right panel: Normalized fluorescence intensity of DDX4 and γH2AX along the dorsal–ventral axis. The range of the x-axis represents the distance from the outer edge to the middle of the ovary. For each group, at least five random linear fluorescence intensity profiles were measured and the shaded regions around the curves depict the 95% confidence intervals

informative gene modules that showed a cluster-specific pattern (Fig. 3d); for example, modules 9 and 10 (M9 and M10) gathered genes that were specifically expressed at the early stage of meiosis, while M2 and M5 gathered genes that were specifically expressed at the meiotic stage, including *SYCP3*, *SYCP1*, and *MEIOB* (Fig. 3c and Additional file 4: Table S3). Alternately, M1, M3, and M4 gathered genes that were specifically expressed at the oocyte stage (including *ZP3*, *ZP4*, and *OOEP*). To gain further insight into gene interactions across the functionally diverse gene modules, we constructed a protein–protein interaction (PPI) network using stage-specific module genes (Additional file 1: Fig. S3b). The results unveiled a complex regulatory network mediating the progression of early oogenesis in pigs. For example, *MEIOB* and *SPDYA* were enriched in the meiotic stage, which is consistent with the fact that *MEIOB* and *SPDYA* are indispensable regulators for the proper progression of murine meiotic prophase I [21, 22].

After dissecting the developmental gene expression landscape underlying early porcine oogenesis, we next investigated this process in the spatial context. Deconvolution of germ cells on the ST chip revealed the remarkable spatial distributions of germ cells at different developmental stages (Fig. 3e), underscoring their distinct spatial patterning at the cellular scale. Specifically, mitotic germ cells and early meiotic germ cells were more numerous in the ovarian surface and outer region of the ovarian cortex across the four developmental time points. Meanwhile, the meiotic germ cells were less abundant in the outer region of the ovarian cortex but gradually increased in abundance along the cortical-medulla axis. Intriguingly, for those germ cells that became oocytes, the early oocyte stage occurred in the boundary of the cortex and medulla region, while late-stage oocytes gradually entered the medulla. Overall, the spatial deconvolution of germ cells unveiled the corticomedullary gradients of early oogenesis.

To further validate our analysis, we performed a whole-mount staining assay using germ cell marker DDX4 and the leptotene stage of meiotic germ cell marker γH2AX to locate germ cells that initiated the meiotic program at various stages (Fig. 3f, left panel) [10, 23]. Consistent with our ST deconvolution assay, it was observed that germ cells at E45 and E55 showed high abundance in both the cortex and medulla regions of the ovary. However, by E65 and E75, it can be observed that germ cells showed the highest abundance in the cortex region. Similarly, DDX4 and γH2AX double-positive meiotic germ cells also significantly changed in spatial context. To provide an in-depth understanding of the cellular dynamics along the C-M axis across various developmental time points, we further evaluated the fluorescence intensity along the C-M axis (Fig. 3f, right panel). Through this analysis, it was observed that the γH2AX signal showed similar levels along the C-M axis in the E45 and E55 ovaries, while in the E65 to E75 ovaries, it was observed that the γH2AX signals peaked in the inner cortex and decreased in the medulla region. Besides, to further verify our analysis, we performed ST sequencing on the same E65 ovarian tissue using a platform with higher resolution (BMKMANU S1000; spot size, ~ 10 μm) (Additional file 1: Fig. S3c) [24]. Consistent with our Visium ST deconvolution at E65, visualization of the spatial location of *ZP3*-positive oocyte using the S1000 platform at E65 also confirmed its expression in the inner cortex (Additional file 1: Fig. S3d). Together, we successfully recapitulated porcine germ cell development at single-cell resolution and also elucidated the spatial distribution patterns of germ cells within the ovarian tissue of pigs.

Cross-species analysis of ST reveals conservation in oogenic programs and spatial location patterns between pigs and humans

After delineating the spatial location characteristics of porcine germ cells during early oogenesis, we next performed a cross-species analysis to provide an in-depth understanding of the spatial regulation of mammalian oogenesis. To this end, we retrieved a ST slide of human ovaries at 19 postconceptional weeks recently reported by Garcia-Alonso et al. [19], and then compared the spatial location pattern of germ cells during various stages of oogenesis with porcine ST data at E65 (Fig. 4a).

Similar to fine-scale cell type characterization in pigs, we first identified homologous cell clusters during the early stages of oogenesis according to cell cluster-specifically expressed genes (Additional file 1: Fig. S4a–b). To identify comparable molecular states between species during early oogenesis, we used 1:1 orthologous genes and compared stage-specifically expressed genes across species. Notably, through these analyses, we characterized the conserved gene programs (FGC_mitotic, 11.5%; Oogonia_STRA8, 6.3%; Oogonia_meiotic, 16%; Pre_oocyte, 6.8%; Oocyte, 10.1% overlapped genes) during the various stages of oogenesis (Additional file 1: Fig. S4c, top panel), and functional enrichment of stage-conserved genes also unveiled conserved signaling pathways involved in mammalian oogenesis (Additional file 1: Fig. S4c, bottom panel). For example, germ cells at the Oogonia_STRA8 stage significantly enriched in GO terms of "response to retinoic acid," a key molecule involved in meiosis initiation [25], further indicating their fate en route to meiosis. While for the germ cells at the Oogonia_meiotic stage, these conserved orthologous genes significantly enriched in GO terms of "meiotic nuclear division" and "female gamete generation." Notably, a meta-analysis of stage-conserved marker genes unveiled a low proportion of shared genes and a comparison of stage-enriched GO terms also showed different enrichment of GO terms, suggesting that the process of oogenesis is orchestrated by stage-specific gene expression programs (Additional file 1: Fig. S4d–e).

In addition to exploring the conserved gene expression programs, we further investigated the expression levels of 5-methylcytosine (5mC) and 5-hydroxymethylcytosine (5hmC) in porcine ovaries at the E55 and E75 stage of development as previous work by Fan et al. demonstrated that human female germ cells en route to early oogenesis undergo global DNA demethylation [26]. Consistent with the human scenario, co-staining of germ cell marker DDX4 with 5mC and 5hmC unveiled that 5mC and 5hmC signals were not detectable in DDX4-positive cells and were predominantly expressed in surrounding gonadal somatic cells in both E55 and E75 porcine ovaries (Fig. 4b, c). These results together further unveil that, in addition to the conserved gene expression programs, the epigenetic reprogramming pattern during early oogenesis is also conserved between humans and pigs.

Next, to investigate whether the corticomedullary gradients of early oogenesis are conserved between pigs and humans, we explored the spatial location pattern of germ cells at various stages of oogenesis based on ST data (Fig. 4d). The results showed that germ cells at the FGC_mitotic and Oogonia_STRA8 stages are predominantly located at the outer cortex, while germ cells that entered the Oogonia_meiotic stage showed the highest abundance in the inner region of the ovary. For germ cells at the Pre_oocyte stage, these germ cells showed a clear location at the inner cortex, while in humans, these cells
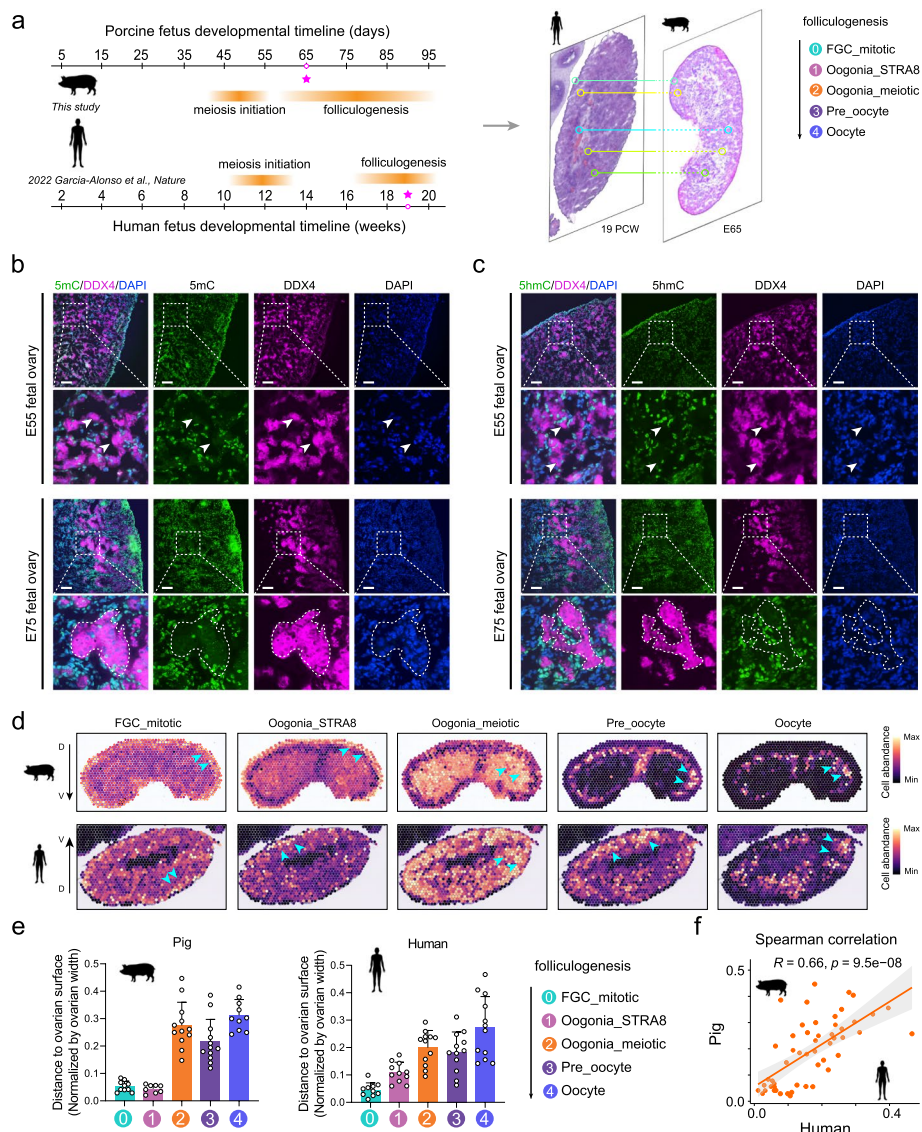
Fig. 4 Cross-species comparative analysis of ovarian ST data between pigs and humans. **a** A brief diagram illustrating the timeline of oogenesis progression between pigs and humans, and sampling time point used for cross-species analysis. **b** Immunofluorescence for 5-methylcytosine (5mC, green) and DDX4 (magenta) in E55 and E75 fetal ovaries. Scale bars, 100 μm. **c** Immunofluorescence for 5-hydroxymethylcytosine (5hmC, green) and DDX4 (magenta) in E55 and E75 fetal ovaries. Scale bars, 100 μm. **d** Comparison of the spatial location of germ cells at different stages of oogenesis in the spatial context between pigs and humans. Arrows indicate the localization of representative high-abundance cell populations. **e** Comparative analysis of the relative spatial distance from germ cells to the ovarian surface in pigs and humans. The y-axis represents the relative distance normalized by ovarian width (along the dorsal–ventral axis). **f** Spearman correlation analysis of the spatial location of germ cells at different stages of oogenesis between pigs and humans

are mainly located at the inner cortex and outer medulla region, with a higher abundance in the inner cortex region. By the Oocyte stage, the location of these germ cells between pigs and humans showed a similar location pattern, predominantly located in the outer medulla region. Besides, we statistically analyzed their relative spatial location pattern at various stages (Fig. 4e). By evaluating the relative distances (normalized by ovarian width) of germ cells to the ovarian surface, it was observed that the process of

early oogenesis in both pigs and humans showed a corticomedullary gradient location of germ cells. Furthermore, we found a significant spearman correlation in the corticomedullary gradient of oogenesis between pigs and humans ($R = 0.66$, $p = 9.5e - 08$) (Fig. 4f). Together, these data not only unveil conservative gene expression programs and epigenetic reprogramming patterns during early oogenesis between pigs and humans but also highlight the conservation in the spatial dynamics throughout the early oogenesis stages in both species.

Unraveling the spatial–temporal characteristics of two granulosa cell lineages during porcine ovarian development using ST

In the developing ovary, granulosa cells crucially interact with germ cells to form the fundamental functional unit of the ovary, known as the ovarian follicle [27]. Therefore, we next extracted granulosa cell lineage and reperformed cell clustering analysis using UMAP; a total of 10 cell clusters were identified (Fig. 5a). By analyzing cell clusters specifically expressed genes, we found that clusters 4, 6, and 7 expressed a higher level of *OSR1* (Additional file 1: Fig. S5a–b), a recently identified wave I pregranulosa cell marker in humans [19]; we therefore termed these clusters as wave I lineage pregranulosa cells (PreGC_I). Furthermore, we found that insulin-like growth factor 2 (*IGF2*) was present at high levels in the PreGC_I (Additional file 1: Fig. S5b), but not in other pregranulosa cells. A recent study by Keshet et al. demonstrated that *IGF2* promotes the differentiation of human embryonic stem cells into granulosa cells [28], thus indicating a critical role of *IGF2* in PreGC_I cell fate commitment in pigs. For clusters 3, 5, and 9, these cells showed high-level expression of *KRT19* and *LHX9* (Additional file 1: Fig. S5b). *KRT19* is known as an epithelial cell marker [29], while *LHX9* is a transcription factor in the LIM homeobox domain gene family and has been demonstrated to be a marker of undifferentiated granulosa cells [30, 31]. A recent murine study also suggests that EPG cells originate from ovarian surface epithelium (OSE) and ingress cortically to associate with cortical germ cells [4]; we, therefore, termed these cells as OSE cells. For the remaining cell clusters 0, 1, 2, and 8, we named these cells as epithelium-derived wave II lineage pregranulosa cells (PreGC_II) according to their increased expression of *WNT6* (cell states 2-1-0-8) and relatively high expression of *KRT19* (Additional file 1: Fig. S5b).

Furthermore, we performed trajectory inference analysis to infer cell state transitions within the granulosa lineages using CellRank [32]. CellRank provides directional information inferred from RNA velocity [33] and can be utilized to gain in-depth insight into the initial, intermediate, and terminal populations in complex scRNA-seq data. Noteworthy, CellRank identified initial states at the bottom of OSE cluster 3 (Fig. 5a, right panel), and two major terminal states toward different cell fates, including OSE cluster 5 and PreGC_II cluster 0. Of all OSE cell populations, we found that OSE cluster 5 showed higher expression of cell proliferation marker *MKI67* (Additional file 1: Fig. S5a), suggesting their mitotically active nature, while OSE cluster 9 showed steady states as revealed by RNA velocity analysis. For PreGC_II cell fate, consistent with a murine scenario, CellRank analysis unveiled a developmental trajectory from OSE to PreGC_II, which represented wave II granulosa cell fate commitment. Next, we analyzed latent time gene expression dynamics along the PreGC_II cell fate commitment (Fig. 5b). The results showed that canonical WNT signaling molecules *WNT6* and *WNT4*, and RA
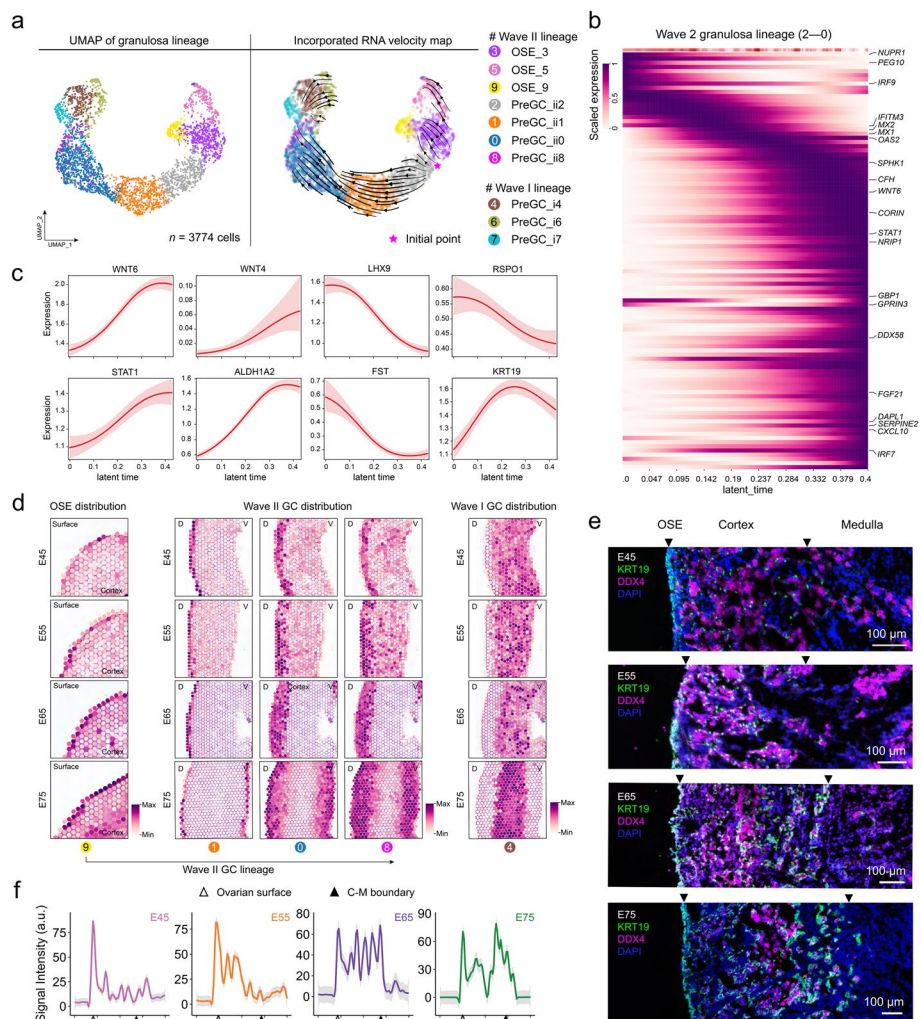
Fig. 5 Characterization of pregranulosa cell developmental trajectory and their spatial location pattern using ST. **a** Fine-scale characterization of pregranulosa cell heterogeneity and inference of pregranulosa cell developmental trajectory by CellRank. *n* indicates the number of cells analyzed and the pentagram represents the initiation point of differentiation identified by CellRank. **b** Smoothed gene expression trends of the top 100 genes whose expression correlates with wave II pregranulosa cell lineage; genes were ranked from top to bottom according to their expression pattern in latent time. **c** Representative marker gene expression trend along the wave II granulosa cell developmental trajectory (latent time). **d** Estimated cell abundances (color intensity) of two main pregranulosa lineage subtypes across four developmental time points. **e** Characterization of the spatial dynamics of wave II granulosa cells in porcine ovaries from E45 to E75 using KRT19 (green) and DDX4 (magenta). The sections for each stage represent magnifying images of ovarian sections along the dorsal–ventral axis. Scale bars, 100 μm. **f** Comparative analysis of the fluorescence signal intensity of KRT19 at different stages along the dorsal–ventral axis. The range of the x-axis represents the distance from the outer edge to the middle of the ovary. For each group, at least five random linear fluorescence intensity profiles were measured and the shaded regions around the curves depict the 95% confidence intervals

synthesis enzyme *ALDH1A2* [34] showed an increased trend along latent time (Fig. 5c). Conditional knockout of WNT signaling molecules in mice has been demonstrated to inhibit pregranulosa cell differentiation into granulosa cells and impaired female fertility [35]; these results together emphasize a conserved role for WNT signaling molecules in porcine pregranulosa cell fate commitment. In addition, the upregulation of *ALDH1A2*

in PreGC_II suggests its potential role in initiating meiotic programs in germ cells via the classical RA-*Stra8* pathway. Consistently, immunofluorescence of ALDH1/2 unveiled that the expression level of ALDH1/2 increases as development progresses (Additional file 1: Fig. S5c). By E75, it was observed that the ALDH1/2 staining signals are predominantly located around the DDX4-positive germ cells, particularly in the inner cortex of the ovary. Together with our ST deconvolution of meiotic germ cells and immunofluorescence analysis (Fig. 3e–f), which indicate that meiotic germ cells are predominantly located in the inner cortex region, these results further support our hypothesis.

Furthermore, we observed upregulated expression of *STAT1*, suggesting a role of the JAK/STAT signaling pathway in PreGC_II cell fate commitment [36]. For downregulated genes, undifferentiated granulosa cell markers *LHX9*, *RSPO1*, and *FST* were identified (Fig. 5c). In agreement with this, a recent study in humans shows that wave II cortical pregranulosa cells are independent of RSPO1/WNT4-β-catenin signaling [19]. We further explored module gene expression patterns within porcine pregranulosa cell subtypes (Additional file 1: Fig. S5d) and identified three major categories of modules (M12 and M13 for OSE populations; M7, M10, and M18 for wave II pregranulosa cells; M3 for wave I pregranulosa cells) that showed lineage-specific enrichment (Additional file 1: Fig. S5e). Through such analysis, we unveil the gene expression landscape underlying granulosa cell fate commitment and gain an in-depth understanding of the cellular and genetic foundations orchestrating ovarian granulosa cell fate commitment in pigs.

After dissecting pregranulosa cell heterogeneity, we next explored spatial characteristics of the granulosa cell lineage. We first performed cell-type deconvolution and observed that OSE populations were mainly located at the ovarian surface in the porcine ovary (Fig. 5d, left panel), and showed increased cell abundance as development advanced. At E45, PreGC_I cells are extensively distributed in the medulla with some in the inner cortex region; with developmental progress, PreGC_I cells gradually ingress inward through the medulla region and increase in cellular abundance, ultimately resting in the central medulla (Fig. 5d, right panel). This is of particular interest as PreGC_I cells are known to associate with wave I medullary follicles in mice [3, 37]. As we generated the developmental trajectory of PreGC_II from OSE, this enabled us to further explore the spatial trajectory of PreGC_II in situ. To this end, we analyzed the spatial location of three cell clusters en route to PreGC_II fate, including cluster 1 (early states), cluster 0 (intermediate states), and cluster 8 (terminal states); the results showed that cluster 1 collocated with OSE populations (Fig. 5d, middle panel), further confirming their origin from the OSE population. As PreGC_II fate commitment proceeded, we observed that these cells ingressed cortically, reaching the outer border of the medullary PreGC_I by E75. Consistent with recent work by Niu and Spradling, lineage tracing of epithelium-derived EPG in mice demonstrates similar cellular kinetics [4].

Notably, epithelium-derived PreGC_II exhibited a gradual ingression toward the center medulla as oogenesis progressed, and they ultimately became widely distributed in the cortex. Through co-staining of KRT19 (OSE and early PreGC_II marker) and DDX4 at various stages, it was observed that KRT19 signals at E45 showed a punctate staining pattern in the cortex region (Fig. 5e–f). By the E55 stage, the staining pattern of KRT19 increased in density. However, when reached E65 and E75, we observed a distinct KRT19 staining pattern characterized by confluent signals, especially in the

boundary regions near the cortex and medulla. Furthermore, it can also observed in the boundary regions between the ovarian cortex and medulla, KRT19 staining signals showed obvious confluent signals encircling the punctate DDX4 signals, indicating the early stage of ovarian follicle assembly. Combining our aforementioned findings from ST that germ cells en route to meiosis showed a corticomedullary gradient distribution pattern in the developing porcine ovary, these data strongly suggest that the differentiation of pregranulosa cell fate is associated with the progression of early oogenesis in pigs.

Spatial characteristics of major somatic cell types during porcine ovarian development

In addition to germ cells and granulosa cells, we further analyzed the spatial distribution patterns of GI and Sm cells at a higher resolution, as these two cell types showed characteristic distribution in the porcine ovary, indicating a potential role in orchestrating ovarian microenvironments. To this end, we reanalyzed GI and Sm cells using UMAP at a higher resolution; the results generated 11 cell clusters (Fig. 6a). For cell cluster 7, those cells expressed a higher level of smooth muscle cell markers, including *RGS5*, *ITGA1*, and *ACTA2* (Additional file 1: Fig. S6a, top panel) [13]. The remaining cell clusters expressed higher levels of canonical steroidogenic lineage markers, including *PDGFRA*, *DCN*, and *OGN* (Additional file 1: Fig. S6a, bottom panel), indicating their GI identity [19]. Notably, the projection of the RNA velocity vectors in the UMAP plot unveiled two main velocity streams, indicating two different cellular states. Comparing differentially expressed genes between these two cell states revealed that cell clusters 4, 8, 9, and 10 expressed higher levels of cell proliferation markers, including *TOP2A*, *HMGB2*, and *CENPF* (Fig. 6b), indicating a proliferative state. The remaining cell states (cell clusters 0, 1, 2, 3, 5, 6) showed a decreased expression of undifferentiated GI marker *TCF21* (Additional file 1: Fig. S6b) [19], thus indicating a differentiating state.

We next employed Hotspot to identify gene modules of correlated genes in different cell fates, and a total of 10 functionally diverse gene modules were identified (Fig. 6c). Projection of these gene modules into the UMAP plot revealed that modules 4 and 6 were specifically enriched in the Sm cell clusters, and gathered Sm cell marker *RGS5* and transcription factor *HEY2*, a key regulator of Sm response to growth factors (Fig. 6c and Additional file 1: Fig. S6c) [38]. GO enrichment of Sm module genes enriched GO terms related to muscle development, further indicating their identity (Additional file 1: Fig. S6d). For the proliferative state of GI cells (cell clusters 4, 8, 9, and 10), modules 2, 5, and 7 were specifically enriched and gathered a series of cell proliferation markers, including *TOP2A* and *MKI67*. Alternately, for the differentiating state (cell clusters 0, 1, 2, 3, 5, 6), modules 8, 9, and 10 were enriched, and these modules gathered genes including GI marker *LUM* and cellular RA-binding protein 1 (*CRABP1*), a mediator of non-canonical activities of RA [39].

We next explored the spatial distribution of these cells by mapping these cell clusters into ST (Fig. 6d). Notably, we also observed that the spatial location of these somatic cells changed with the progression of development from E45 to E75. For example, the differentiating lineage cells and the proliferative state cells identified by RNA velocity were randomly distributed in the ovary at E45 and E55, while in the E65 we observed these cells showed a higher abundance mainly in the cortex region and increased their abundance when reached E75. Similarly, Sm cells exhibited a similar
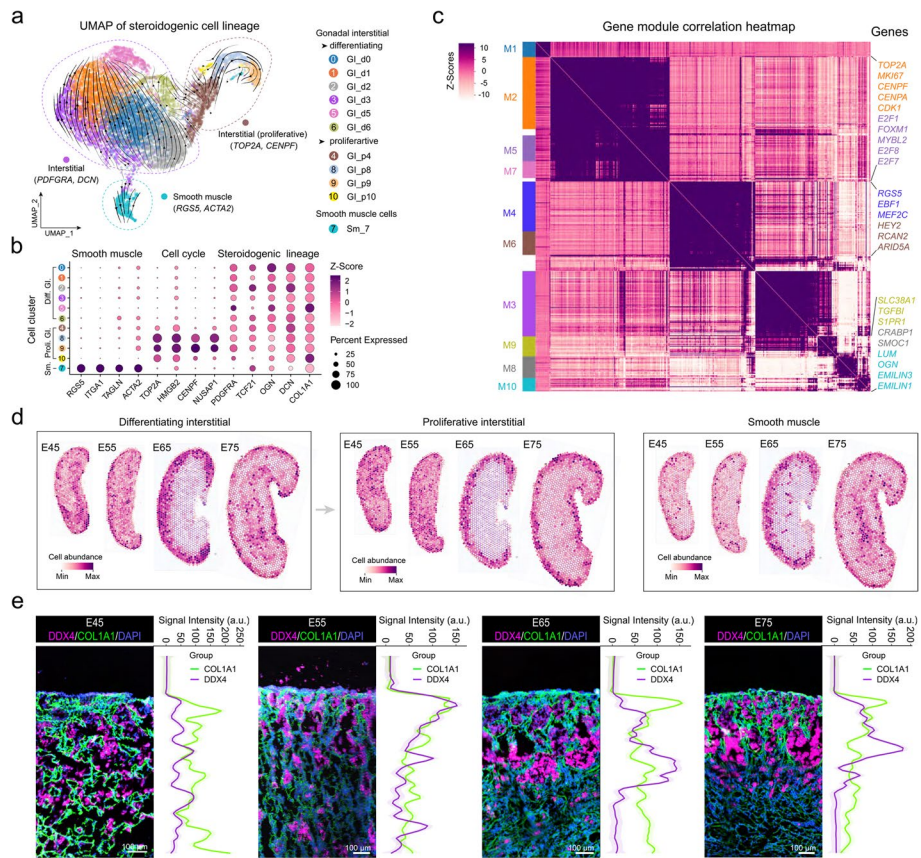
Fig. 6 Characterization of steroidogenic cell lineage heterogeneity and spatial location pattern using ST. **a** Fine-scale characterization of steroidogenic cell lineage cell heterogeneity. Arrows in the UMAP plot indicate RNA velocity vectors. GI, gonadal interstitial; Sm, smooth muscle. **b** Dot plot illustrating representative marker gene expression across steroidogenic cell lineage. **c** Correlation heatmap of functional gene modules identified by Hotspot analysis. Representative module genes were colored-coded in the right panel. **d** Estimated cell abundances (color intensity) of GI and Sm cell subtypes across four developmental time points. **e** Comparative analysis of the fluorescence signal intensity of COL1A1 (green) and DDX4 (magenta) at different stages along the dorsal–ventral axis. From top to bottom represents the distance from the outer edge to the middle of the ovary. The fluorescence intensity in each image is presented from top to bottom on the right side of each image. For each group, at least five random linear fluorescence intensity profiles were measured and the shaded regions around the curves depict the 95% confidence intervals. Scale bars, 100 μm

cell location pattern, with some peak signals observed in the medulla region at E75 (Fig. 6d, right panel). Besides, we performed an immunofluorescence staining assay using steroidogenic lineage marker COL1A1 and germ cell marker DDX4 at various time points (Fig. 6e), and the results showed that COL1A1 signals showed no difference between cortex and medulla region at E45. As the development progresses, the staining signal of COL1A1 increases in the cortex region, together with the clustered distribution of germ cells at E65. Furthermore, it can be observed that in the medulla region of E65 and E75 ovaries, COL1A1-positive cells showed loose and reticular distribution patterns, while germ cells showed punctate location among these cells. Together, these results indicate that steroidogenic lineage cells also exhibit dynamic

Ge *et al. Genome Biology*   (2025) 26:2

Page 16 of 27

spatial location patterns during early oogenesis in pigs, indicating a potential role in shaping the ovarian microenvironment essential for early oogenesis.

Spatial co-occurrence analysis revealed distinct microenvironments in the cortical and medullary region, highlighting a critical role in regulating germ cell fates

After delineating the spatiotemporal characteristics of major cell types in the developing porcine ovary, we next reasoned how changes in the spatial microenvironments affect cell fate determination in the developing ovary. To this end, we first performed non-negative matrix factorization (NMF) of the cell type abundance to investigate the spatial co-occurrence of cells in the developing ovary (Fig. 7a) [17]. After NMF decomposition, we obtained four major cellular compartments (factors 0, 1, 3, and 4). Notably, factor 0 accounts for cellular compartments of medulla origin, as revealed by spatial mapping of germ cells from the Pre_oocyte and Oocyte stages. Factor 4 accounts for the cellular compartment of the cortical region, as revealed by spatial
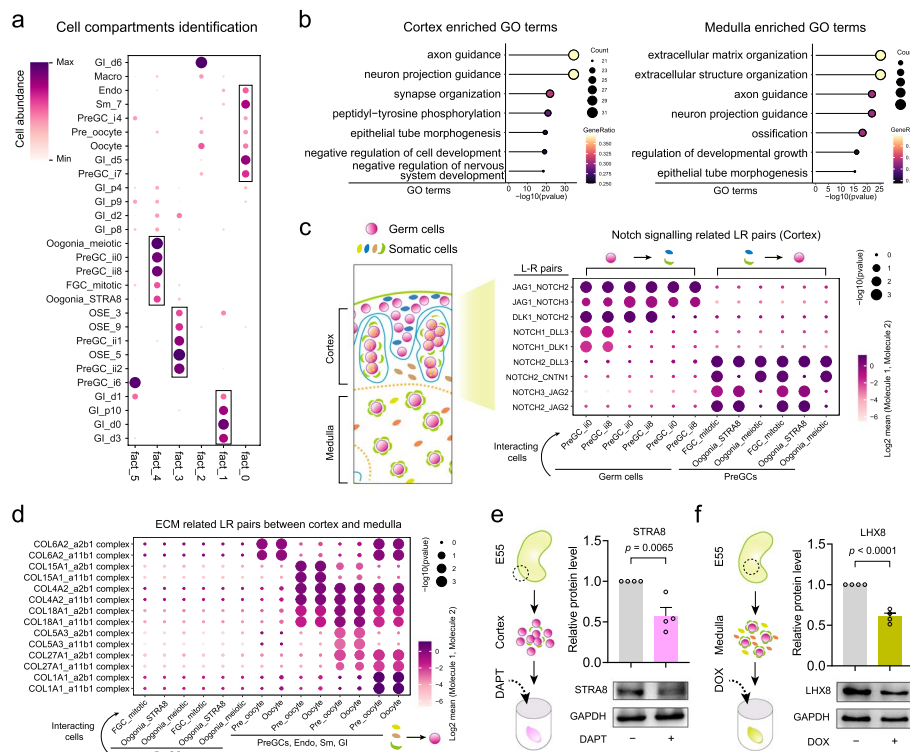

Fig. 7 Comparison of cell–cell communication patterns between the ovarian cortex and medulla. **a** Cell type co-occurrence analysis using NMF. Columns indicate NMF components while rows indicate estimated weights of cell types. **b** GO enrichment analysis of intercellular communication patterns between cortical and medullary cell populations in the porcine ovary. **c** Dot plot showing representative NOTCH signaling related L-R pairs between pregranulosa cells and germ cells in the cortex region. **d** Dot plot showing representative ECM-related L-R pairs between germ cells and somatic cells in the medulla region. **e** The effects of the NOTCH signaling inhibitor DAPT on the expression of meiotic marker STRA8 during in vitro culture of cortex tissues isolated from E55 fetal ovaries. Ovarian tissues were harvested after 10 days in vitro suspension culture. Data are presented as mean ± SEM. **f** The effects of the matrix metalloproteinase inhibitor doxycycline on the expression of folliculogenesis marker LHX8 during in vitro culture of medulla tissues isolated from E55 fetal ovaries. Ovarian tissues were harvested after 10 days in vitro suspension culture. Data are presented as mean ± SEM

mapping of the mitotic to meiotic germ cells. For factor 3, the decomposed cell types were composed of cells in the ovarian surface, and factor 1 was composed mainly of GI populations.

Notably, the application of NMF decomposition successfully characterized the germ cell compartments located in the cortex and medulla and unveiled which somatic cells were co-located with the germ cells of different spatial origins. These findings together provided an unparalleled opportunity for further exploration of how somatic microenvironments affect germ cell fate in situ. Therefore, we then performed cell–cell communication analysis based on the spatial co-occurrence of different cell types. Overall, we observed distinct patterns of cell–cell communication between germ cells and somatic cells in the cortex and medulla (Additional file 1: Fig. S7a). To provide a comprehensive understanding of the functionality of cell–cell communication patterns, we performed GO enrichment analysis using CellphoneDB identified ligand-receptor (L-R) pairs between germ cells and somatic cells in different regions (Fig. 7b). Through this analysis, we observed different functional enrichment results of cell–cell communication patterns between the cortex and medulla region. For example, in the cortex region, "axon guidance" and "neuron projection guidance" were the top enriched GO terms using L-R pairs generated between germ cells and somatic cells. In contrast, for L-R pairs in the medulla region, "extracellular matrix organization" and "extracellular structure organization" were the top enriched GO terms. These results together indicate that there are differences in the intercellular communication patterns between germ cells and somatic cells in the cortex and medulla regions.

Specifically, we observed that L-R pairs in the cortex region significantly enriched the NOTCH signaling pathway (Fig. 7c and Additional file 1: Fig. S7a). For example, we observed that both PreGC_ii0 and PreGC_ii8 expressed NOTCH signaling mediator *NOTCH2*, while its ligands *DLK1* and *JAG1* were expressed in germ cells en route to meiosis. Notably, this observation is reminiscent of a murine scenario where conditional deletion of *Notch2* in granulosa cells resulted in a decreased number of primordial follicles [40]. Together, these results further indicate a critical role of *NOTCH2* in early germ cell fate determination in pigs. Moreover, we observed that PreGCs expressed WNT signaling ligand *WNT5A* and its corresponding receptor, including *SFRP1*, and *FZD3* were expressed in the germ cells, suggesting a role of WNT signaling during early meiotic progression in pig oogonia (Additional file 1: Fig. S7a). In contrast, in the medulla region (located by Pre_oocyte and oocyte), cell–cell communication analysis unveiled that germ cells at the oocyte stage expressed ligands involved in primordial follicle assembly, including *BMP4* [39] and *BDNF* [40], while their corresponding receptors, including *BMPR1A*, *BMPR1B*, and *SORT1*, were expressed by PreGC i4 and PreGC i7. Notably, we found that somatic cells in the medulla region express a range of ECM proteins, while this is not the situation in the cortex region (Fig. 7d). For example, *COL4A2* was observed in all these cell types, while *COL15A1* was detected in endothelial cells, and *COL6A2* was expressed in GI cells. For Sm cells, *COL18A1*, *COL5A3*, and *COL27A1* were observed to be expressed. These data together suggest a critical role of ECM proteins in regulating porcine oogenesis.

To further verify our cell–cell communication analysis, we next reasoned whether supplementation of NOTCH signaling inhibitor DAPT and matrix metalloproteinase inhibitor doxycycline would affect germ cell fates using ovarian tissues isolated from E55 ovarian cortex and medulla under in vitro conditions [41]. To this end, we dissected cortical and medullary tissues from the E55 fetal ovary (Additional file 1: Fig. S7b), and histological and immunofluorescence staining verified that these ovarian tissues were accurately isolated from the ovarian cortex and medulla (Additional file 1: Fig. S7c–d). These tissues were then subjected to in vitro culture and after 10 days treatment of DAPT, it was observed that the expression level of the meiotic marker STRA8 in cortical ovarian tissue was significantly decreased (Fig. 7e), while it was not the case for the ovarian tissues from the medulla (Additional file 1: Fig. S7e). In contrast, after 10 days treatment of with matrix metalloproteinase inhibitor doxycycline, we observed a decreased expression level of the folliculogenesis marker LHX8 [42], with no comparable effect observed in cortical tissues (Fig. 7f and Additional file 1: Fig. S7f). Taken together, these data further support our cell–cell communication analysis in a spatial context and highlight an underappreciated role of ovarian microenvironments in regulating germ cell fates.

Discussion

Advances in scRNA-seq and ST technologies have provided an unparalleled opportunity to explore spatial dynamic gene expression profiles of different cell types during in situ gonad development. Here, for the first time, we report a comprehensive single-cell atlas of porcine gonad development covering the early stage of oogenesis. Fine-scale analysis of germ cell populations recapitulates the developmental trajectory of oogenesis at single-cell resolution, which provides an in-depth understanding of the gene expression cascades mediating early porcine oogenesis. Furthermore, we detailed the gene expression landscape underlying wave II pregranulosa cell fate determination through developmental trajectory inference. Most importantly, we have characterized the spatial distribution dynamics of different cell lineages en route to fate commitment in the spatial context. Our work here unveils the underappreciated characteristics of ovarian microenvironment establishment and also provides novel insight into how ovarian architecture is associated with female fertility.

Intriguingly, fine-scale analysis of germ cell populations successfully recapitulated germ cell developmental trajectory en route to folliculogenesis, and an in-depth analysis of their gene expression pattern provides in-depth insight into the genetic foundations of porcine oogenesis. Through mapping germ cells of different developmental stages in situ, a corticomedullar pattern for porcine oogenesis was noted, which was different from recent observations in mice [10]. Using three-dimensional in toto imaging to monitor meiotic initiation waves in mice, Soygur et al. reported a radial wave of meiotic initiation followed by an A-P wave of meiosis in the murine ovary. However, in the current study, we found that the meiotic program during porcine oogenesis showed a corticomedullar pattern. Confirming such analysis, labeling the leptotene stage of meiotic germ cells using γH2AX at murine E12.5 unveiled an anterior-radial staining pattern, while in our current study, co-staining of DDX4 and γH2AX unveiled an inner cortical distribution of double-positive cells, suggesting a different migratory pattern for germ

Ge *et al. Genome Biology*   (2025) 26:2

Page 19 of 27

cells en route to meiosis for pigs, as compared to mice. Notably, in humans, recent work by Luz et al. reports a similar germ cell distribution pattern in the developing human ovary, namely mitotic germ cells located in the outer cortex and meiotic germ cells located mainly in the inner cortex, while in the medulla, *FIGLA*-positive oocytes were observed, suggesting a corticomedullar pattern. Furthermore, our cross-species analysis of ST data between pigs and humans also unveiled conservative spatial dynamics of germ cells in the spatial context. However, current ST technology failed to resolve spatial dynamics at "real" single-cell resolution (for example, each spot in the current study contained ∼ 26 cells); therefore, how murine ovarian architecture affects germ cell spatial dynamics remains to be explored. In this regard, the rapid advancement of ST technology and cell characterization algorithms will likely help address this question in the near future. Besides, the differences in germ cell spatial dynamics in mice compared to pigs and humans is a question of particular notice, and analyzing cross-species cellular dynamics in a spatial context may provide insight into how mammalian oogenesis is regulated in a spatial context and will broaden our knowledge of early oogenesis in mammals.

Although germ cell spatial dynamics in mice is different compared with pigs and humans, the spatial dynamics of pregranulosa cells seem to be conserved between mice and pigs. Using lineage tracing experiments in mice, Niu and Spradling recently unveiled that BPG (or PreGC_I) is extensively located both in the cortex and medulla of the ovary at E12.5; furthermore, as development advances, BPG cells in the cortex were displaced as the EPG cells (or PreGC_II) ingressed cortically. Labeling porcine EPG using KRT19 also confirmed its gradual ingression from the outer cortex to the inner cortex from E45 to E75 (Fig. 5e), indicating a conserved mechanism regulating spatial dynamics in pregranulosa cells. Notably, both lineage tracing and representative marker expression staining failed to account for the cellular heterogeneity within pregranulosa cells en route to migration. To this end, combined analysis of pregranulosa cell developmental trajectory to identify different cellular states en route to differentiation, and spatial mapping of these cellular states in situ, provided insights into the spatial trajectory of pregranulosa cell fate commitment in a spatial context. For wave II granulosa cells of epithelial origin, the spatial distribution of the EPG cells from the ovarian surface toward the medulla region corresponded to the initial states and terminal states of EPG differentiation identified by CellRank. In other words, as the differentiation process of EPG advanced, their corresponding spatial location may be closer to the medulla. Together with corticomedullar gradients of oogenesis, and colocation of pre-granulosa cells and germ cells (Fig. 5e), these data emphasize the critical role of pregranulosa cells in regulating germ cell fate commitment.

Furthermore, through spatial co-occurrence analysis and cell–cell communications analysis, we unveiled substantial L-R pairs between germ cells and somatic cells in the ovarian cortex and medulla during early oogenesis in pigs; these data provide a valuable resource for further investigation of intracellular communication regarding regulating early oogenesis. Notably, we observed a series of conserved L-R pairs between humans and pigs, for example, significant enrichment of ECM remodeling proteins in the medulla, suggesting a conserved role of intracellular communication across mammalian

early oogenesis; future cross-species analysis of these L-R pairs will help to identify critical intracellular signals that regulate female fertility.

Conclusions

In conclusion, the current study gained in-depth insights into the spatial organization of ovarian architecture and is a valuable resource for understanding spatiotemporal gene expression cascades. By employing cross-species comparative analysis, we have elucidated conserved spatial dynamical characteristics in the early oogenesis process between humans and pigs. This distinction from model organisms such as mice implies that pigs represent an ideal model for investigating the spatial features of early oocyte development in humans. Through cell–cell communications analysis, we explored how the somatic microenvironment mediates cell fate commitment in germ cells. These results broaden our current understanding of early oogenesis and will have meaningful implications for reproductive medicine.

Methods

Experimental samples

All experimental procedures involving animal experiments were approved by the Ethics Committee of Qingdao Agricultural University (No. SYXK-20220–021). Pregnant pigs (three-way hybrid strains of Landrace, Large White, and Duroc) were bred via artificial insemination, and porcine embryos were collected from a local livestock farm. Porcine ovarian samples were collected at 45, 55, 65, and 75 days post-fertilization. After rinsing with ice-cold PBS solution to remove contaminated blood, the ovarian tissues were then embedded with an OCT medium (Sakura, 4583) and were immediately placed onto a block of dry ice to freeze the tissues. Ovarian sections were prepared using a Leika CM1950 cryostat at a thickness of 15 μm.

Porcine embryo collection and single-cell preparation for scRNA-seq

First, the ovarian tissues were rinsed in ice-cold PBS solution three times to remove any contaminants. Then, the tissues were torn into smaller pieces before being incubated with 2 mg/ml collagenase solution (Sigma, C5138) for 10 min at 37 °C. Subsequently, the samples were centrifuged to remove the supernatant collagenase solution and ice-cold PBS solution containing 0.04% bovine serum albumin (BSA, Sigma, V900933) was then added. Samples were gently dispersed using a 1-ml pipette, and the resulting cell suspensions were washed three times with ice-cold PBS solution containing 0.04% BSA. To prepare single-cell pellets for scRNA library construction, the cell suspensions were filtered through a 45-μm cell strainer and cell viability was determined by TC20 automated cell counter (TC20, BioRad) via trypan blue staining. Samples with cell viability > 85% were processed for downstream analysis, and at least 60,000 cells were harvested for each sample.

Ge *et al. Genome Biology*   (2025) 26:2

Page 21 of 27

10 × Chromium scRNA‑seq library preparation and gene expression matrix generation

We used a 10 × Genomics' Chromium Next GEM Single Cell 3′ Kit v3.1 (10 × Genomics, PN‑1000268) for cDNA library preparation. All procedures were performed according to the manufacturer's instructions. For single cell barcoding, a 10 × Genomics Chromium barcoding system (10 × Genomics) was utilized and about 7000 cells were captured for each library. Subsequently, an Illumina NovaSeq 6000 sequencer was used to generate raw sequencing reads, and gene expression matrixes were generated using the CellRanger software (v6.1.2, 10 × Genomics). Sscrofa11.1 (Ensemble assembly) was used as the reference genome.

10 × scRNA‑seq data analysis

To perform basic quality control and visualization, we used the Seurat (v4.0.1) package to process the output gene expression matrices from CellRanger pipeline. Briefly, the gene expression matrices from CellRanger were firstly loaded into Seurat using the *Read10X* function, then the *CreateSeuratObject* function was used to create a Seurat object, and low‑quality cells were filtered out using the following parameter: *min.cells* = 3, *min.features* = 200, *nFeature_RNA* > 1000, *nFeature_RNA* < 6000 (5000 for E65), and *percent.mt* < 0.5. We further used the *DoubleFinder* package to remove potential doublets; all parameters were set at default values [43], and the identified doublets were filtered out using the *subset* function. To integrate samples of different batches and remove the batch effect, we used the *Harmony* package and all parameters were set at default values [44]. Subsequently, we performed uniform manifold approximation and projection (UMAP) for dimension reduction. Cell clusters were identified using the *FindClusters* (resolution = 0.5) function in Seurat, and cluster‑specific expressed genes were identified using the *FindAllMarkers* function with the following parameters: *Wilcoxon rank-sum test, logfc.threshold = 0.25 and min. pct = 0.25.*

10 × Visium section preparation and sequencing

We used 10 × Visium chip for ST analysis, and all procedures were performed according to the manufacturer's instructions. Briefly, OCT‑embedded frozen porcine ovaries were first transferred to a cryostat for 4 h before sectioning. Ovarian samples were then sectioned at a thickness of 10 μm and immediately underwent hematoxylin–eosin staining to determine the appropriate section layers. The final sections were then mounted onto Visium slides and then moved on to the permeabilization step. Before permeabilization, to gauge the optimized time, we tested a series of times ranging from 3 to 30 min (6‑time points) and selected 28 min for porcine ovary permeabilization. Next, the resulting cDNA libraries were sequenced using an Illumina NovaSeq 6000 sequencer, and the raw sequencing reads files were further processed using the Spaceranger software (v1.3.1, 10 × Genomics) to generate raw counts of each spot.

ST data deconvolution

Cell2location was used for Visium data deconvolution in this study as it outperforms other deconvolution algorithms [18]; all parameters were set using the default

values unless indicated. Briefly, after cell type characterization of the integrated Seurat object, it was then transformed into a *Scanpy* object for estimation of reference cell type signatures [45]. Reference cell type signatures were calculated with the Cell-2location package using a negative binomial regression model; all parameters were set to default values. To determine the optimized training size, the *max_epochs* parameters were determined using the ELBO loss history plot and were increased unless leveled off by the end of the training. After reference cell type signature characterization, we moved on to the spatial mapping step. For Cell2location spatial mapping, we first manually determined *N_cells_per_location* hyperparameters (indicating the number of cells per spot) using the Loupe Browser (v6.1.0, 10 × Genomics), and at least 100 spots were randomly selected for each slide. For the porcine ovary samples here, *N_cells_per_location* was set to 22, and *detection_alpha* parameters were set to 10 because we observed high technical variability in RNA detection sensitivity within the slide. The spatial location of different cell types was then visualized using the *sc.pl.spatial* function. To identify the spatial co-occurrence of cell types, we identified cellular compartments using non-negative matrix factorization (NMF) with the default parameters.

RNA velocity analysis

We used *Velocyto* and *scVelo* packages for RNA velocity analysis and all parameters were set to default values [33, 46]. First, the output files from the CellRanger pipeline were processed with *Velocyto* to generate loom files containing spliced/unspliced matrices using the *velocyto run10x()* function. After loading the merged loom files, we subset the merged loom object using Seurat-derived metadata information and UMAP coordinates to construct the *anndata* object. Then, RNA velocity was calculated using the *scv.tl.velocity* function with the *stochastic* mode, and velocity vectors were visualized using the *scv.pl.velocity_embedding_stream* function.

Trajectory inference of scRNA-seq

We used the Cellrank package for trajectory inference analysis [32]. First, after loading the *anndata* object, genes that had less spliced/unspliced counts were filtered out and were further normalized using the *scv.pp.filter_and_normalize* function. Then, RNA velocity was calculated using the dynamical model from the *scVelo* package. To identify the terminal states, the *cr.tl.terminal_states* function was used with the following parameters: *weight_connectivities*=0.2, *n_states*=3, while the initial state was identified using the *cr.tl.initial_states* function. The computing of the cell fate maps was then performed using the *cr.tl.lineages* function. Subsequently, to compute lineage driver genes, the *cr.tl.lineage_drivers* function was used and gene expression trend along latent time was visualized using the *cr.pl.gene_trends* function based on a general additive model (GAM). Finally, the heatmap of the top 100 cell fate driver genes was visualized using the *cr.pl.heatmap* function with default settings.

Orthologous gene transformation

The orthologues of porcine genes were identified using the *biomaRt* (v2.38.0) R package [47].

Ge *et al. Genome Biology*   (2025) 26:2

Page 23 of 27

Cell–cell communication analysis

To identify cell–cell communication, we used CellphoneDB (v3.1.0) software with an updated database containing 2046 extra manually curated ligand-receptor pairs and all parameters were set using the default values [19, 48]. Briefly, we first transformed porcine genes into corresponding human 1:1 orthologue genes using *biomaRt* (v2.38.0) software [47]. Then, the normalized expression values of different cell types were extracted and subjected to CellphoneDB analysis using the statistical mode. Visualization of ligand-receptor pairs was performed using the *ktplots* (v1.2.1, https://github.com/zktuong/ktplots) package.

Protein–protein interaction (PPI) network construction

To perform PPI network analysis, we retrieved interacting genes from the STRING database (https://string-db.org/) using default settings. The interacting network was then visualized using Cytoscape software (v3.9.1, https://cytoscape.org/).

Gene ontology enrichment analysis

To provide insight into the biological functions of cluster-specific expressed genes, we used Metascape for gene ontology enrichment with default parameters [36].

Identification of stage-specific gene modules

To identify highly correlated gene modules for each cell cluster, we used Hotspot (v1.1.1) to compute cell cluster-specific informative genes [20]. Briefly, after filtering low-quality cells and genes with low abundance, we used the *hotspot.Hotspot* function to create the Hotspot object from *anndata* object. Subsequently, we used the *hs.compute_autocorrelations* function to compute autocorrelations for each gene, and pair-wise local correlations between these genes were further calculated using the *hs.compute_local_correlations* function. Genes were grouped into different modules using the *hs.create_modules* function using the following parameter: fdr_threshold = 0.05. Finally, to plot the module correlation heatmap, we used the *hs.plot_local_correlations()* function.

Immunofluorescence

For immunofluorescence analysis, the OCT-embedded frozen porcine ovarian tissues were firstly sectioned using a cryostat at a thickness of 8–10 μm at − 20 °C. Slides were then subjected to air drying at room temperature for 1 h; then, after two washes with PBS solution, slides were washed three times with TBST buffer (Tris-buffered saline with 0.1% Tween® 20 Detergent). Slides were subsequently fixed with 4% PFA solution for 10 min at room temperature. After that, blocking was performed using a PBS solution containing 1% BSA and 0.1% Triton X-100 in a wet box for 30 min. Primary antibodies diluted in the blocking buffer were added to the slides and were incubated at 4 °C overnight. The next morning, after three washes with TBST solution, corresponding secondary antibodies were added and the slides were incubated at 37 °C for 1 h. After three washes with PBS solution, the slides were mounted using

a Vectashield mounting medium (Vector Laboratories), and images were taken using an LSM 900 confocal microscope.

Image analysis and quantification

Images were analyzed using Fiji-ImageJ software [49]. To evaluate the cortical-medullar intensity, the normalized gray values of spilt channels were measured using the ImageJ analysis tool.

Western blotting analysis

Western blotting was performed as we previously described [50]. Briefly, the harvested ovarian tissues were firstly washed with PBS solution and then lysed on ice using RIPA lysis solution (Beyotime, P0013B). After that, the resulting suspensions were subjected to gel electrophoresis using a 12% SDS-PAGE gel, with electrophoresis performed at 80 V for 20 min and then at 120 V for 2.5 h. Then, the target proteins were transferred to the polyvinylidene difluoride membranes (Millipore, ISEQ00010) with a Bio-Rad Trans-Blot system (Bio-Rad). Following a blocking step with 5% BSA (Solarbio, A8020), the gel bands were incubated with the corresponding primary antibodies and secondary antibodies overnight at 4 °C. All primary and secondary antibodies used in the current study were listed in Additional file 5: Table S4. Chemiluminescence was performed using a BeyoECL star chemiluminescence kit (Beyotime, P0018S) and images were taken under a Tanon-5200 imaging system (Tanon Scientific Inc., 5200).

Ovarian tissues in vitro culture

The ovarian culture methods were adapted from previous reports [51], with some modifications. Briefly, after slaughtering at a local abattoir, pig embryos were promptly transferred to the laboratory, and the obtained fetuses were then washed three times using saline containing 1% antibiotics. After that, the fetal ovaries were mechanically isolated and washed three times with DMEM/F12 (Gibco, C11330500BT) media to remove containments. To obtain cortex and medulla tissues, the ovarian surface tissues were mechanically separated under a stereomicroscope using forceps, and the obtained cortex tissues were split into small pieces (approximately 1/50 of the ovarian volume). After that, the medulla tissues were obtained and were cut into small pieces of the same size to the cortex tissues. The resulting ovarian tissues were then subjected to floating culture using a low-binding U bottom 96-well plate. The culture medium consisted of Advanced MEM (Gibco, 12,492,013) containing 10% FBS (Gibco, 10,437,028), 2 mM GlutaMAX (Gibco, 226,810), 150 μM L-ascorbic acid (Sigma, SLBN3833V), 1 × penicillin streptomycin solution (SparkJade, DTBTQ), 10 μM Y-27632 dihydrochloride (TOCRIS, 1254), and 55 μM 2-mercaptoethanol (Amresco, 0482). Half of the medium was changed every 2 days. To block the NOTCH signaling pathway and ECM protein production during in vitro culture, 100 μM γ-secretase inhibitor DAPT (Selleck, S2215) and 20 nM matrix metalloproteinase inhibitor doxycycline (Selleck, S5159) were supplemented to the culture media as previously reported [41, 52].

Statistical analysis

All quantification plots were presented as mean $\pm$ SEM, and a two-tailed, unpaired *t*-test was used for comparing groups of two using GraphPad Prism (version 5.01).

Supplementary Information

The online version contains supplementary material available at https://doi.org/10.1186/s13059-024-03464-8.

Additional file 1. Fig. S1-S7

Additional file 2. Table S1. Signature genes for each cell type identified by Seurat.

Additional file 3. Table S2. Germ cell stage-specific expressed markers.

Additional file 4. Table S3. Germ cell module genes identified by HotSpot.

Additional file 5. Table S4. All primary and secondary antibodies used in this study.

Additional file 6. Review history.

Review history
The review history is available as Additional file 6.

Peer review information
Veronique van den Berghe was the primary editor of this article and managed its editorial process and peer review in collaboration with the rest of the editorial team.

Authors' contributions
W. G. and W. S. conceived this project; W. G., Y.-L. N., Y.-K. L., Li-Li, H. W., W.-W. L., T. Q., Y.-N. F., and Y.-Q. F. performed the experiments; W. G. and H. W. performed bioinformatics analysis; J. L., J.-J. W., X.-F. S., S.-F. C., and Lan-Li discussed and integrated the data; W. G. wrote the manuscript; and W. S. supervised the study. All coauthors provided feedback on the final manuscript.

Authors' information
Authors and affiliations
College of Life Sciences, Key Laboratory of Animal Reproduction and Biotechnology in Universities of Shandong, Qingdao Agricultural University, Qingdao 266109, China. Wei Ge, Yi-Lin Niu, Yu-Kang Li, Li Li, Han Wang, Wen-Wen Li, Tian Qiao, Jun-Jie Wang, Xiao-Feng Sun, Shun-Feng Cheng, Lan Li, Wei Shen. Laboratory of Animal Reproductive Physiology and Disease, College of Veterinary Medicine, Qingdao Agricultural University, 266109, Qingdao, China. Yan-Ni Feng. School Hospital, Qingdao Agricultural University, 266109, Qingdao, China. Yu-Qing Feng Central Laboratory of Qingdao Agricultural University, Qingdao Agricultural University, Qingdao 266109, China. Jing Liu

Data availability
Raw sequencing data used for scRNA-seq have been deposited to the Genome Sequence Archive under accession number CRA011422 [53]; raw sequencing data used for ST have been deposited to the Genome Sequence Archive under accession number CRA011100 [54]. HE images used for ST, as well as the main scripts for data processing and analysis, are available on Zenodo (HE images: https://doi.org/10.5281/zenodo.14286941 [55] and main scripts: https://doi.org/10.5281/zenodo.14286998 [56]) and a GitHub repository (https://github.com/Flyingcattle/Pig_Spatial) [57] under the CC BY 4.0 license.

Declarations

Ethics approval and consent to participate
All experimental procedures involving animal experiments were approved by the Ethics Committee of Qingdao Agricultural University (No. SYXK-20220–021).

Consent for publication
Not applicable.

Competing interests
The authors declare that they have no competing interests.

References

1. Zhang J, Yan L, Wang Y, Zhang S, Xu X, Dai Y, et al. In vivo and in vitro activation of dormant primordial follicles by EGF treatment in mouse and human. Clin Transl Med. 2020;10: e182.
2. Grosbois J, Bailie EC, Kelsey TW, Anderson RA, Telfer EE. Spatio-temporal remodelling of the composition and architecture of the human ovarian cortical extracellular matrix during in vitro culture. Hum Reprod. 2023;38:444–58.
3. Zheng W, Zhang H, Gorre N, Risal S, Shen Y, Liu K. Two classes of ovarian primordial follicles exhibit distinct developmental dynamics and physiological functions. Hum Mol Genet. 2014;23:920–8.
4. Niu W, Spradling AC. Two distinct pathways of pregranulosa cell differentiation support follicle formation in the mouse ovary. Proc Natl Acad Sci U S A. 2020;117:20015–26.
5. Richardson BE, Lehmann R. Mechanisms guiding primordial germ cell migration: strategies from different organisms. Nat Rev Mol Cell Biol. 2010;11:37–49.
6. Molyneaux KA, Stallock J, Schaible K, Wylie C. Time-lapse analysis of living mouse germ cell migration. Dev Biol. 2001;240:488–98.
7. Cordeiro MH, Kim SY, Ebbert K, Duncan FE, Ramalho-Santos J, Woodruff TK. Geography of follicle formation in the embryonic mouse ovary impacts activation pattern during the first wave of folliculogenesis. Biol Reprod. 2015;93:88.
8. Bowles J, Knight D, Smith C, Wilhelm D, Richman J, Mamiya S, et al. Retinoid signaling determines germ cell fate in mice. Science. 2006;312:596–600.
9. Koubova J, Menke DB, Zhou Q, Capel B, Griswold MD, Page DC. Retinoic acid regulates sex-specific timing of meiotic initiation in mice. Proc Natl Acad Sci U S A. 2006;103:2474–9.
10. Soygur B, Jaszczak RG, Fries A, Nguyen DH, Malki S, Hu G, et al. Intercellular bridges coordinate the transition from pluripotency to meiosis in mouse fetal oocytes. Sci Adv. 2021;7: eabc6747.
11. Greenbaum MP, Iwamori N, Agno JE, Matzuk MM. Mouse TEX14 is required for embryonic germ cell intercellular bridges but not female fertility. Biol Reprod. 2009;80:449–57.
12. Saiti D, Lacham-Kaplan O. Mouse germ cell development in-vivo and in-vitro. Biomark Insights. 2007;2:241–52.
13. Ge W, Wang JJ, Zhang RQ, Tan SJ, Zhang FL, Liu WX, et al. Dissecting the initiation of female meiosis in the mouse at single-cell resolution. Cell Mol Life Sci. 2021;78:695–713.
14. Duan H, Cheng T, Cheng H. Spatially resolved transcriptomics: advances and applications. Blood Sci. 2023;5:1–14.
15. Moor AE, Itzkovitz S. Spatial transcriptomics: paving the way for tissue-level systems biology. Curr Opin Biotechnol. 2017;46:126–33.
16. Zhao E, Stone MR, Ren X, Guenthoer J, Smythe KS, Pulliam T, et al. Spatial transcriptomics at subspot resolution with BayesSpace. Nat Biotechnol. 2021;39:1375–84.
17. Kleshchevnikov V, Shmatko A, Dann E, Aivazidis A, King HW, Li T, et al. Cell2location maps fine-grained cell types in spatial transcriptomics. Nat Biotechnol. 2022;40:661–71.
18. Li B, Zhang W, Guo C, Xu H, Li L, Fang M, et al. Benchmarking spatial and single-cell transcriptomics integration methods for transcript distribution prediction and cell type deconvolution. Nat Methods. 2022;19:662–70.
19. Garcia-Alonso L, Lorenzi V, Mazzeo CI, Alves-Lopes JP, Roberts K, Sancho-Serra C, et al. Single-cell roadmap of human gonadal development. Nature. 2022;607:540–7.
20. DeTomaso D, Yosef N. Hotspot identifies informative gene modules across modalities of single-cell genomics. Cell Syst. 2021;12(446–456): e449.
21. Guo R, Xu Y, Leu NA, Zhang L, Fuchs SY, Ye L, et al. The ssDNA-binding protein MEIOB acts as a dosage-sensitive regulator of meiotic recombination. Nucleic Acids Res. 2020;48:12219–33.
22. Chen Y, Wang Y, Chen J, Zuo W, Fan Y, Huang S, et al. The SUN1-SPDYA interaction plays an essential role in meiosis prophase I. Nat Commun. 2021;12:3176.
23. Malki S, van der Heijden GW, O'Donnell KA, Martin SL, Bortvin A. A role for retrotransposon LINE-1 in fetal oocyte attrition in mice. Dev Cell. 2014;29:521–33.
24. You Y, Fu Y, Li L, Zhang Z, Jia S, Lu S, et al. Systematic comparison of sequencing-based spatial transcriptomic methods. Nat Methods. 2024;21:1743–54.
25. Griswold MD, Hogarth CA, Bowles J, Koopman P. Initiating meiosis: the case for retinoic acid. Biol Reprod. 2012;86:35.
26. Fan X, Moustakas I, Torrens-Juaneda V, Lei Q, Hamer G, Louwe LA, et al. Transcriptional progression during meiotic prophase I reveals sex-specific features and X chromosome dynamics in human fetal female germline. PLoS Genet. 2021;17: e1009773.
27. Niu W, Spradling AC. Mouse oocytes develop in cysts with the help of nurse cells. Cell. 2022;185(2576–2590): e2512.
28. Keshet G, Bar S, Sarel-Gallily R, Yanuka O, Benvenisty N, Eldar-Geva T. Differentiation of uniparental human embryonic stem cells into granulosa cells reveals a paternal contribution to gonadal development. Stem Cell Reports. 2023;18:817–28.
29. Kuony A, Michon F. Epithelial markers aSMA, Krt14, and Krt19 unveil elements of murine lacrimal gland morphogenesis and maturation. Front Physiol. 2017;8: 739.
30. Mazaud S, Oreal E, Guigon CJ, Carre-Eusebe D, Magre S. Lhx9 expression during gonadal morphogenesis as related to the state of cell differentiation. Gene Expr Patterns. 2002;2:373–7.
31. Lin YT, Barske L, DeFalco T, Capel B. Numb regulates somatic cell lineage commitment during early gonadogenesis in mice. Development. 2017;144:1607–18.
32. Lange M, Bergen V, Klein M, Setty M, Reuter B, Bakhti M, et al. Cell Rank for directed single-cell fate mapping. Nat Methods. 2022;19:159–70.
33. La Manno G, Soldatov R, Zeisel A, Braun E, Hochgerner H, Petukhov V, et al. RNA velocity of single cells. Nature. 2018;560:494–8.

Ge *et al. Genome Biology*   (2025) 26:2

Page 27 of 27

34. Chassot AA, Le Rolle M, Jolivet G, Stevant I, Guigonis JM, Da Silva F, et al. Retinoic acid synthesis by ALDH1A proteins is dispensable for meiosis initiation in the mouse fetal ovary. Sci Adv. 2020; 6:eaaz1261.

35. Habara O, Logan CY, Kanai-Azuma M, Nusse R, Takase HM. WNT signaling in pre-granulosa cells is required for ovarian folliculogenesis and female fertility. Development. 2021;148:dev198846.

36. Zhou Y, Zhou B, Pache L, Chang M, Khodabakhshi AH, Tanaseichuk O, et al. Metascape provides a biologist-oriented resource for the analysis of systems-level datasets. Nat Commun. 2019;10:1523.

37. Mork L, Maatouk DM, McMahon JA, Guo JJ, Zhang P, McMahon AP, et al. Temporal differences in granulosa cell specification in the ovary reflect distinct follicle fates in mice. Biol Reprod. 2012;86:37.

38. Shirvani SM, Mookanamparambil L, Ramoni MF, Chin MT. Transcription factor CHF1/Hey2 regulates the global transcriptional response to platelet-derived growth factor in vascular smooth muscle cells. Physiol Genomics. 2007;30:61–8.

39. Nhieu J, Lin YL, Wei LN. CRABP1 in non-canonical activities of retinoic acid in health and diseases. Nutrients. 2022;14: 1528.

40. Xu J, Gridley T. Notch2 is required in somatic cells for breakdown of ovarian germ-cell nests and formation of primordial follicles. BMC Biol. 2013;11: 13.

41. Palomino-Morales R, Torres C, Perales S, Linares A, Alejandre MJ. Inhibition of extracellular matrix production and remodeling by doxycycline in smooth muscle cells. J Pharmacol Sci. 2016;132:218–23.

42. Pangas SA, Choi Y, Ballow DJ, Zhao Y, Westphal H, Matzuk MM, et al. Oogenesis requires germ cell-specific transcriptional regulators Sohlh1 and Lhx8. Proc Natl Acad Sci U S A. 2006;103:8090–5.

43. McGinnis CS, Murrow LM, Gartner ZJ. DoubletFinder: doublet detection in single-cell RNA sequencing data using artificial nearest neighbors. Cell Syst. 2019;8(329–337): e324.

44. Korsunsky I, Millard N, Fan J, Slowikowski K, Zhang F, Wei K, et al. Fast, sensitive and accurate integration of single-cell data with Harmony. Nat Methods. 2019;16:1289–96.

45. Wolf FA, Angerer P, Theis FJ. SCANPY: large-scale single-cell gene expression data analysis. Genome Biol. 2018;19:15.

46. Bergen V, Lange M, Peidli S, Wolf FA, Theis FJ. Generalizing RNA velocity to transient cell states through dynamical modeling. Nat Biotechnol. 2020;38:1408–14.

47. Durinck S, Spellman PT, Birney E, Huber W. Mapping identifiers for the integration of genomic datasets with the R/Bioconductor package biomaRt. Nat Protoc. 2009;4:1184–91.

48. Efremova M, Vento-Tormo M, Teichmann SA, Vento-Tormo R. Cell PhoneDB: inferring cell-cell communication from combined expression of multi-subunit ligand-receptor complexes. Nat Protoc. 2020;15:1484–506.

49. Schindelin J, Arganda-Carreras I, Frise E, Kaynig V, Longair M, Pietzsch T, et al. Fiji: an open-source platform for biological-image analysis. Nat Methods. 2012;9:676–82.

50. Ge W, Sun YC, Qiao T, Liu HX, He TR, Wang JJ, et al. Murine skin-derived multipotent papillary dermal fibroblast progenitors show germline potential in vitro. Stem Cell Res Ther. 2023;14:17.

51. Mizuta K, Katou Y, Nakakita B, Kishine A, Nosaka Y, Saito S, et al. Ex vivo reconstitution of fetal oocyte development in humans and cynomolgus monkeys. EMBO J. 2022;41: e110815.

52. Li SY, Bhandary B, Gu X, DeFalco T. Perivascular cells support folliculogenesis in the developing ovary. Proc Natl Acad Sci U S A. 2022;119: e2213026119.

53. Ge W. scRNA seq of E45 to E75 porcine ovary. Genome Sequence Archive. https://ngdc.cncb.ac.cn/gsa/browse/CRA011422 (2024).

54. Ge W. Spatial transcriptomic of E45 to E75 porcine ovary. Genome Sequence Archive. https://ngdc.cncb.ac.cn/gsa/browse/CRA011100 (2024).

55. Ge W. HE images of E45-E75 fetal porcine ovaries. Zenodo. 2024. https://doi.org/10.5281/zenodo.14286941.

56. Ge W. Scripts used for analyzing single-cell and spatial transcriptomic data of porcine ovarian tissues during the E45-E75. Zenodo. 2024. https://doi.org/10.5281/zenodo.14286998.

57. Ge W. Pig_Spatial. Github. 2024. https://github.com/Flyingcattle/Pig_Spatial.

Publisher's Note

Springer Nature remains neutral with regard to jurisdictional claims in published maps and institutional affiliations.